Optica Applicata, Vol. LII, No. 1, 2022
DOI: 10.37190/oa220108

Interferogram blind denoising using deep residual learning for phase-shifting interferometry

Xiaoqing Xu[1], Ming Xie[2], Song Chen[1], Ying Ji[2], Yawei Wang[2]

[1]Institute of Mold Technology, Changzhou Vocational Institute of Mechatronic Technology, Changzhou 213164, Jiangsu, China

[2]Faculty of Science, Jiangsu University, Zhenjiang 212013, China

*Corresponding author: xxqyzzd@sina.com

The interferogram containing the noises often affects the accuracy of phase retrieval, leading to the degradation of the phase imaging quality. To address this issue, a new interferogram blind denoising (IBD) method based on deep residual learning is proposed. In the presence of unknown noise levels, during the training, the deep residual convolutional neural networks (DRCNN) in the IBD approach is able to remove the latent clean interferogram implicitly, and then gradually establish the residual mapping relation in the pixel-level between the interferogram and the noises. With a well-trained DRCNN model, this algorithm can deal not only with the single-frame interferogram efficiently but also with the multi-frame phase-shifted interferograms collaboratively, while effectively retaining interferogram features related to phase retrieval. Simulation and experimental results demonstrate the feasibility and applicability of the proposed IBD method.

Keywords: interferogram denoising, deep learning, interferometry.

1. Introduction

Phase-shifting interferometry (PSI) is a well-known and useful technique for quantitative phase imaging [1, 2] and high-precision surface topography measurement [3–5]. In PSI, however, the interferogram captured by the CCD inevitably contains the noises owing to the dim field of view, high temperature of the image sensor and unstable environmental disturbances. In general, the noisy interferogram usually affects the accuracy of phase extraction, resulting in the degradation of phase imaging quality. Thus, filtering off the noises from phase-shifted interferogram is an important preprocessing step for making phase retrieval more accurate and robust in PSI. Typically, an iterative method based on an average convolution kernel ones or several times is employed to denoise an interferogram, but this algorithm can cause a blurring effect in the interferogram. In order to cope with this problem, many different algorithms [6–10] have been proposed. In [7], a two-dimensional windowed Fourier filtering (WFF) approach is proposed to reduce the noises in intensity fringe pattern and exponential phase filed, but it may result in the boundary artifacts of denoised interferogram. In [8], a fringe

pattern denoising algorithm is presented using image decomposition, but this method requires a prior knowledge about interferogram divided into different spaces. In [9], a dimensionality-reduction-based denoising algorithm is introduced to suppress the noises of fringe pattern using the singular value decomposition (SVD) method, but this algorithm needs to perform the additional operations of the rotation and a zero padding process. In [10], a well-established block-matching 3D filtering (BM3D) algorithm is proposed for image denoising using the non-local adaptive nonparametric filtering method through grouping and collaborative filtering, but this algorithm firstly needs to estimate the noise levels and aims at general image denoising with certain noise levels. Although all the algorithms above can lead to satisfactory results of image denoising, how to filter off efficiently the noises from the noisy interferogram remains an important problem of a preprocessing step due to the fact that the noises in the interferogram are random and unknown.

Deep learning (DL) originating from an artificial neuron model is a new area in machine learning research [11], in which its core idea is mainly to extract the features of the image associated with the tasks as the input of the support vector machine using the convolutional neural networks (CNN). Recently, DL has been widely used in various fields, such as recognition [12], feature classification [13], cell image segmentation [14, 15], optical image reconstruction and phase recovery [16], dual-wavelength interferogram decoupling [17], digital holographic microscopy [18], and optically trapped particle tracking [19].

In this paper, to address the interferogram with unknown and random noise levels, a novel interferogram blind denoising (IBD) method is proposed using deep residual learning (DRL) strategy. With the well-trained CNN model, the proposed method can establish the residual mapping relation in the pixel-level between the interferogram and noises. In the presence of different blind noise levels, this algorithm can handle not only a single-frame interferogram efficiently but also multi-frame phase-shifted interferograms collaboratively, while retaining the interferogram features associated with phase extraction. The effectiveness and applicability of the proposed IBD method are demonstrated by the simulation and experimental results of the plane wave-front, micro-sphere, complex wave-front, peaks and spherical cap, respectively. To the best of our knowledge, this is the first time that this method is proposed in this paper in PSI.

2. Principle

2.1. Denoising in phase-shifting interferometry

In PSI, the phase-shifted interferogram can be theoretically expressed as

$$I_{\mathrm{R}}(x, y) = a(x, y) + b(x, y)\cos\left[\varphi(x, y) + \delta\right] + \eta(x, y) \tag{1}$$

where x and y are spatial coordinates, $a(x, y)$ and $b(x, y)$ are the dc term and modulation amplitude, $\varphi(x, y)$ and δ denote the phase and random phase shifts, respectively; $\eta(x, y)$ is the blind additive white Gaussian noise (AWGN).

In order to conveniently express the denoising, Eq. (1) can be rewritten as

$$I_R = I_C + \eta \tag{2}$$

where I_C is the noise-free or noise-suppressed interferogram. In general, the goal of interferogram denoising is to filter off the noise η from the noisy interferogram I_R, which can be defined as

$$I_C = I_R - \eta \tag{3}$$

The residual mapping strategy is much easier to be obtained than the original unreferenced mapping, so deep CNN in residual mode has the capability to learn the residual mapping relationship rapidly [20, 21]. Deep CNN can be easily trained and improve the accuracy of interferogram denoising by using this residual learning strategy. In our proposed IBD method, the noisy interferogram I_R is much more like the noise-suppressed interferogram I_C than the noise image η, especially for interferogram with a low blind noise level. Thus, the residual mapping will be much easier to be trained and optimized due to the fact that the end-to-end mapping relation is more like an identity mapping, in the IBD. As a result, we can conclude that the residual learning strategy is very suitable for interferogram denoising.

Thus, to conveniently obtain the residual mapping, Eq. (3) can be rewritten as

$$\eta = I_R - I_C \tag{4}$$

2.2. The architecture of the proposed DRCNN

Based on Eq. (4), the architecture of deep residual convolutional neural networks (DRCNN) is designed for the IBD method, as shown in Fig. 1. In the DRCNN framework, the input is the noisy interferogram I_R, and the output is the noise image η. The framework of the DRCNN consists of four types of blocks, with four different colors. Each block consists of different numbers of convolutional layers. Each layer is composed of different numbers of 3×3 convolutions, each followed by a batch normaliza-

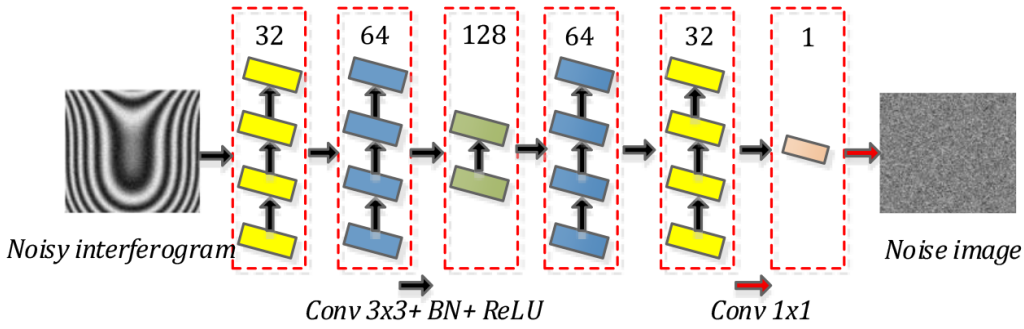

Fig. 1. Architecture of the DRCNN for the IBD method. The number of feature channels is denoted in the red dotted box, respectively.

tion (BN) and a rectified linear unit (ReLU). Suppose the input data volume of the ℓ-th convolutional layer is denoted as x_j^{ℓ}, which can be expressed as

$$\xi_{\ell}(x_j^{\ell}) = \mathrm{ReLU}\left\{\mathrm{BN}\left[\sum\nolimits_{i=1}^{N^{(\ell-1)}}(x_i^{(\ell-1)} * w_{ij}^{\ell} + b_j^{\ell})\right]\right\}, \quad j = 1, 2, ..., N^{(\ell)} \tag{5}$$

where w is the weight, b is the bias, $*$ denotes the convolutional operation, $\xi_{\ell}(\cdot)$ denotes the residual mapping function at the ℓ-th convolutional layer, and $N^{(\ell)}$ is the number of feature channels. The purpose of BN, using both zero mean and unit variance to normalize each BN layer, is to improve the performance of the proposed DRCNN and reduce the internal covariate shift [22], and BN can be defined as

$$\hat{x}_j = \gamma \frac{x_j - \mu[x_j]}{\sqrt{\sigma^2 + \varepsilon}} + \beta \tag{6}$$

where

$$\mu[x] = \frac{1}{N^{(\ell)}} \sum_{j=1}^{N^{(\ell)}} x_j$$

$$\sigma^2 = \frac{1}{N^{(\ell)}} \sum_{j=1}^{N^{(\ell)}} (x_j - \mu[x_j])^2$$

and $\hat{x}_j$ is the output of the BN layer, ε is a regularization parameter, γ is a scaling factor and β is the shifting factor. The ReLU activation alleviates the problem of vanishing gradient and improves the convergence speed of the proposed DRCNN, and the ReLU activation function [23] can be represented as

$$\hbar(x_j) = \max(0, x_j) \tag{7}$$

In Fig. 1, the black arrows denote Conv 3×3+BN+ReLU, and the red arrow is Conv 1×1. To extract multi-channel and high-level features of interferogram from the noisy interferogram, the number of feature channels for each layer in the IBD method is set to be 32, 64, 128, 64, 32 and 1, respectively, which are denoted in the red dotted box. There are 19 convolutional operations in the IBD method.

2.3. DL-based blind denoising and training parameters setting of the DRCNN

With these residual mapping functions in Eq. (5), the residual mapping relation $\xi(\cdot) = \sum_{i=1}^{L=19} \xi_i(\cdot)$ can be obtained through minimizing the loss function $\ell(\Theta)$ between the desired noise images and predicted ones from the noisy inputs, which can be defined by

$$\ell(\Theta) = \frac{1}{W}\sum_{k=1}^{W}\left\|(I_{Rk} - I_{Ck}) - \xi(I_{Rk};\, \Theta)\right\|_2^2 \tag{8}$$

where W is the batch size and Θ is the trainable parameters of the DRCNN.

It is worthy to note that the DRCNN adopts Eq. (4) rather than Eq. (3) for establishing the pixel-wise residual mapping. That is to say, the framework of the DRCNN is designed to output the noise image rather than directly outputting the denoised interferogram. Once the optimal pixel-level residual mapping relation $\xi(\cdot)$ of I_R to η is achieved, the noise image η can be expressed as

$$\eta = \xi(I_R;\, \Theta) \tag{9}$$

Subsequently, by combining Eqs. (3) and (9), the noise-suppressed interferogram I_C can be described as

$$I_C = I_R - \xi(I_R;\, \Theta) \tag{10}$$

During the training in the framework of the DRCNN, the batch size W is 4; the training epochs for this dataset are 50; the learning rate is firstly set to be 1e-3, then it decays from 1e-3 to 1e-7; the adaptive moment estimation (Adam) based optimizer is used to minimize the $\ell(\Theta)$ in Eq. (8) by iterative back-propagation algorithm.

3. Simulations and discussion

3.1. Dataset generation

To verify the feasibility of the IBD method, as shown in Fig. 2, five types of interferograms, including the plane wave-front, micro-sphere, peaks, spherical cap and complex wave-front, are employed as the objects of training and testing. For each type of interferogram, 80 randomly phase-shifted interferograms with the size of 128×128 pixels are generated according to Eq. (1) by setting the parameters as follows: the background term is $a(x, y) = 40\exp[-0.04(x^2 + y^2)] + 90$ and the modulation term is $b(x, y) =$

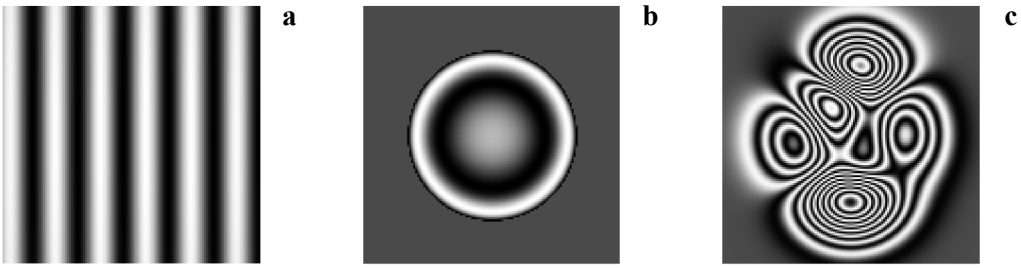

Fig. 2. Five types of interferograms: (**a**) plane wave-front, (**b**) micro-sphere, (**c**) peaks, (**d**) spherical cap and (**e**) complex wave-front.

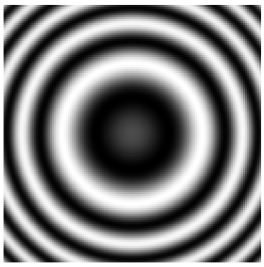

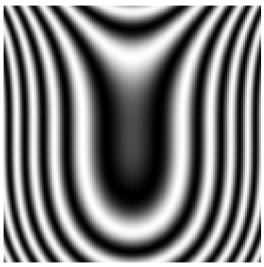

Fig. 2. Continued.

$= 90\exp[-0.04(x^2 + y^2)]$, respectively; δ is a random phase shift in the range from 0 to 2π; the AWGN with zero-mean and standard deviation σ inside the range (0, 40) is arbitrarily added to each phase-shifted interferogram. The dataset consisting of 400 randomly phase-shifted interferograms is utilized to train the DRCNN framework. Note that the test samples are different from those in the training dataset.

3.2. Denoising of single-frame interferogram

To evaluate the performance of a well-trained DRCNN model, 60 interferograms with random phase shifts are employed in the presence of different blind noise levels. Specifically, the value of low blind noise (LBN) is $\sigma = 6$; the value of medium blind noise (MBN) is $\sigma = 22$; the value of high blind noise (HBN) is $\sigma = 38$. To quantitatively evaluate the IBD method, we introduce the peak signal-to-noise ratio (PSNR), which can be defined by

$$\mathrm{PSNR} = 10\log\left\{\frac{(2^n-1)^2}{\frac{1}{MN}\sum_{i=1}^{M}\sum_{j=1}^{N}\left[I_1(i,j)-I_2(i,j)\right]^2}\right\} \tag{11}$$

where M and N respectively denote the size of the interferogram; I_1 is the noise-free interferogram, and I_2 is the interferogram denoised using different algorithms; n is equal to 8.

In the Table, for five types of interferograms, based on Eq. (11), we present the average PSNR results obtained with the IBD, BM3D, WFF and SVD methods in the presence of LBN, MBN and HBN, respectively. It is worthy to note that the default parameters for the BM3D and WFF are used and the number of largest singular values that are not truncated is 10 in the SVD method. For example, in the Table, for the micro-sphere, at LBN, the WFF method has the lowest value of PSNR about 16.82 dB, while the IBD method yields the best value of PSNR about 37.15 dB, resulting in significant improvement of the IBD method by 20.33 dB. It is found from the Table that the IBD method has the highest value of PSNR on most of phase-shifted interferograms compared with the BM3D, SVD and WFF methods, but fails to obtain the best value of PSNR

T a b l e. The average PSNR (dB) results obtained by the IBD, BM3D, SVD and WFF methods for five types of interferograms at LBN, MBN and HBN. The best results are highlighted in bold.

Methods	IBD	BM3D	SVD	WFF
			LBN	
Plane wave-front	**36.17**	34.41	29.29	18.54
Micro-sphere	**37.15**	36.05	25.01	16.82
Peaks	30.16	**32.15**	13.51	11.66
Spherical cap	**36.04**	33.30	31.06	18.42
Complex wave-front	**35.28**	33.52	30.56	12.99
			MBN	
Plane wave-front	**36.00**	34.68	26.69	18.42
Micro-sphere	**35.35**	33.71	22.78	16.56
Peaks	**29.59**	28.06	13.49	11.62
Spherical cap	**35.18**	32.21	25.58	18.37
Complex wave-front	**34.43**	32.78	24.94	12.94
			HBN	
Plane wave-front	**33.10**	32.45	22.84	18.13
Micro-sphere	**31.96**	31.15	20.43	16.32
Peaks	**27.91**	24.90	13.36	11.57
Spherical cap	**32.26**	30.25	21.98	18.05
Complex wave-front	**31.82**	29.84	21.40	12.87

on phase-shifted interferogram of peaks at LBN. Through the analysis of five types of interferograms, one can know that phase-shifted interferograms of peaks possessing multiple closed-interferograms increase the difficulty of recognition of interferogram features in the DRCNN, leading to the unsatisfactory result of interferogram denoising for the IBD method. The simulation results show that the IBD method has better blind denoising performance of single-frame interferogram for different blind noise levels.

3.3. Filtering off the noises from multi-frame phase-shifted interferograms

3.3.1. The plane wave-front

To verify the effectiveness of the proposed IBD method for denoising of the plane wave -front, four noisy interferograms with 0, $\pi/2$, π and $3\pi/2$ phase shifts, one of which is presented in Fig. 3**a**, are used to simultaneously denoise. In Fig. 3**e** the theoretical phase map is shown and in Fig. 3**f** the noisy phase map is presented. Through the calculation, one can know that the root mean square error (RMSE) of the noise in Figs. 3**e** and 3**f** is 0.31 rad. Figures 3**b**–3**d** present one of the denoised interferograms with the IBD, SVD and WFF methods, respectively. Then the phases retrieved from the denoised interferograms with the IBD, SVD and WFF methods are presented in Figs. 3**g**–3**i**, and the corresponding RMSEs are 0.04, 0.19 and 0.11 rad, respectively. Note that their phases are extracted using a standard four-step phase-shift (FSPS) algorithm. Com-

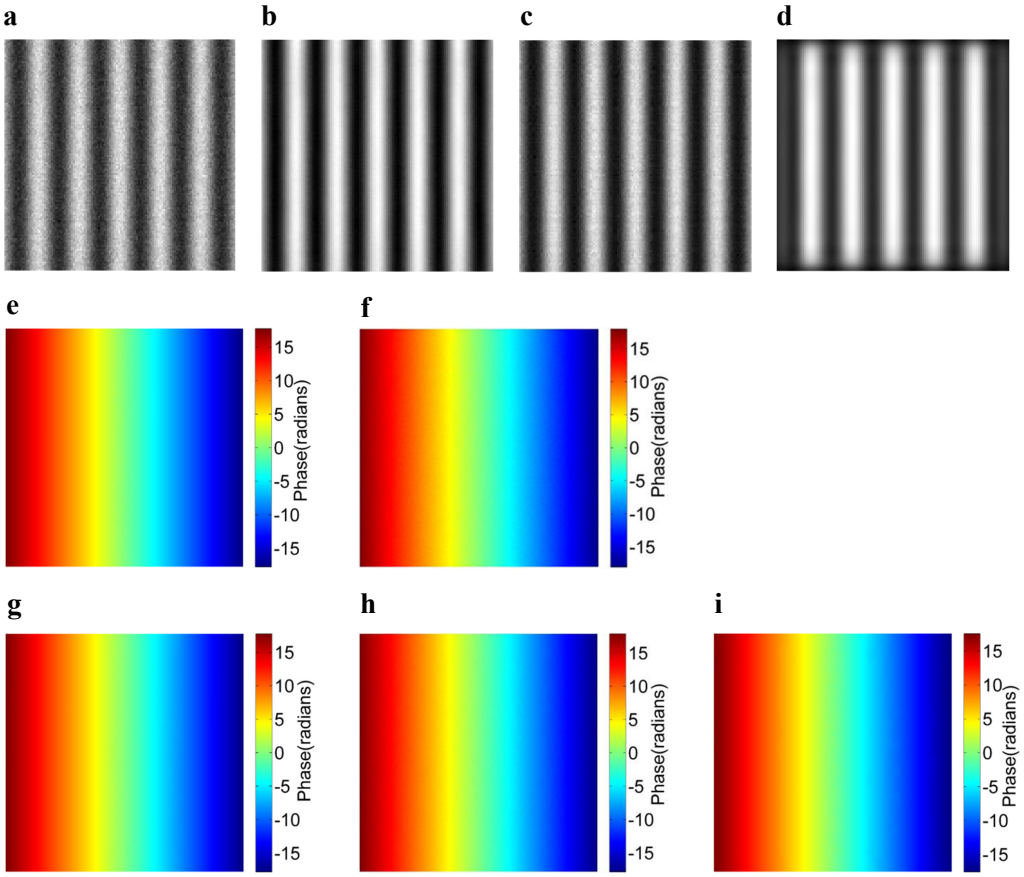

Fig. 3. The plane wave-front. (**a**) The noisy interferogram, (**b**), (**c**) and (**d**) the interferograms denoised with the IBD, SVD and WFF methods, (**e**) and (**f**) the theoretical and noisy phases, (**g**), (**h**) and (**i**) the phases extracted from the interferograms denoised with the IBD, SVD and WFF methods, respectively.

pared with the RMSE of noisy phase, that is 0.31 rad, the values of noise removal for the IBD, SVD and WFF methods are 0.27, 0.12 and 0.20 rad, respectively.

3.3.2. The spherical cap

We employ four noisy interferograms with 0, $\pi/2$, π and $3\pi/2$ phase shifts, one of which is presented Fig. 4**a**, to verify the feasibility of the IBD method for denoising of the spherical cap. One of the interferograms denoised by the IBD, BM3D, SVD and WFF methods is presented in Figs. 4**b**–4**e**, respectively. To compare the blind denoising performance, the theoretical and noisy phases are illustrated in Figs. 5**a** and 5**b**, respectively. The RMSE of the noise in Figs. 5**a** and 5**b** is 0.24 rad through the calculation. The phases extracted from the interferograms denoised with the IBD, BM3D, SVD and WFF methods are shown in Figs. 5**c**–5**f** by using the FSPS algorithm, and the corresponding

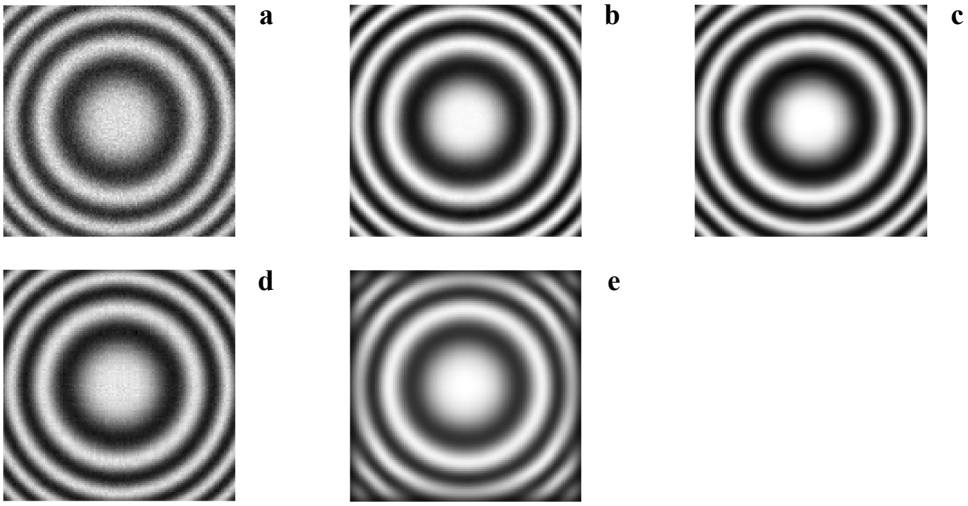

Fig. 4. The spherical cap. (**a**) The noisy interferogram, (**b**), (**c**), (**d**) and (**e**) the interferograms denoised with the IBD, BM3D, SVD and WFF, respectively.

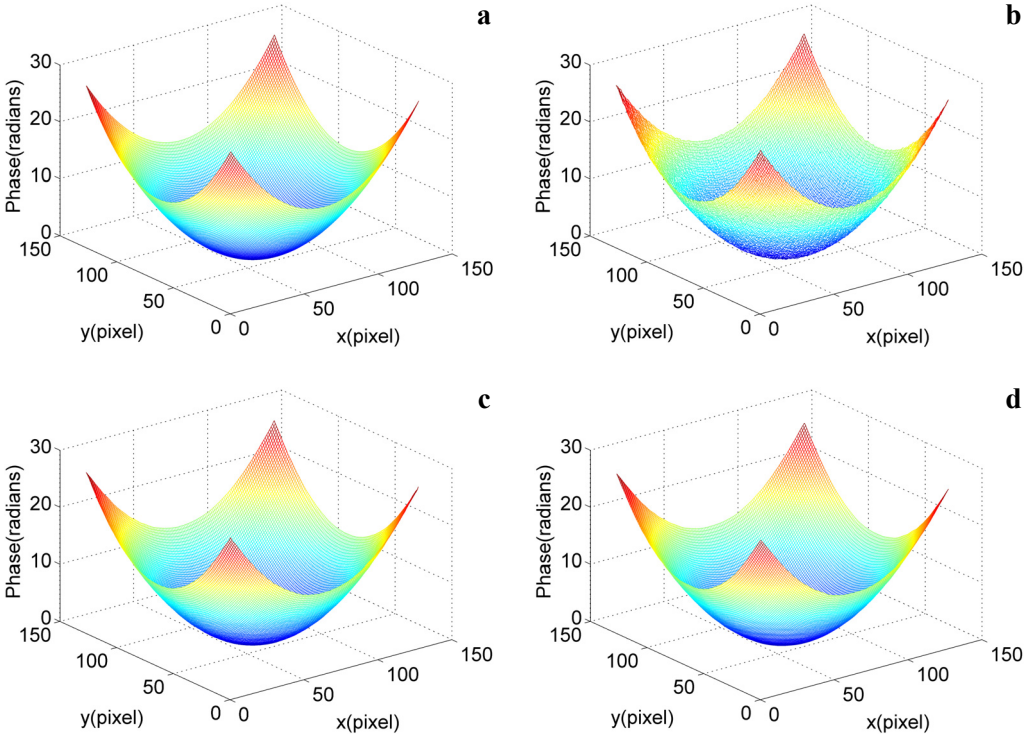

Fig. 5. The spherical cap. (**a**) The theoretical phase, (**b**) the noisy phase, (**c**), (**d**), (**e**) and (**f**) the phases retrieved from the interferograms denoised with the IBD, BM3D, SVD and WFF methods, respectively.

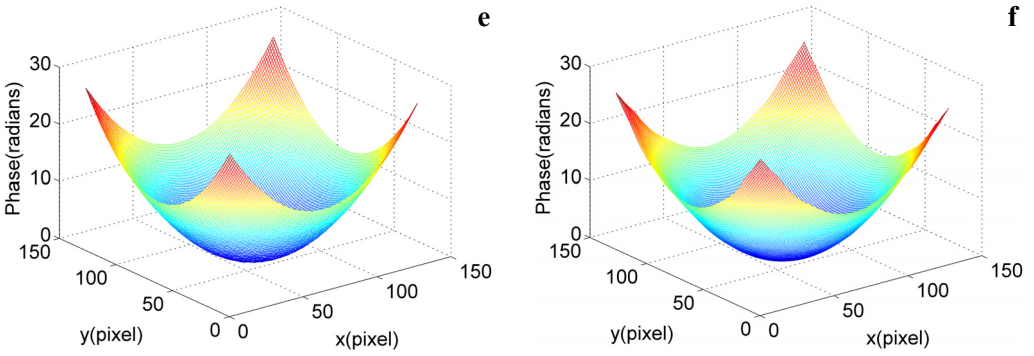

Fig. 5. Continued.

RMSEs are 0.03, 0.05, 0.06 and 0.14 rad, respectively. Compared with the RMSE of noisy phase, that is 0.24 rad, the values of noise removal for the IBD, BM3D, SVD and WFF methods are respectively 0.21, 0.19, 0.18 and 0.1 rad.

3.3.3. The complex wave-front

To demonstrate the feasibility of the IBD method for denoising of the complex wave -front, three noisy interferograms with 0, 2.5 and 4.5 phase shifts are employed to simultaneously filter off the noises, one of which is shown in Fig. 6**a**. Figures 6**d** and 6**e** respectively present the theoretical and noisy phases, and the RMSE of the noise in

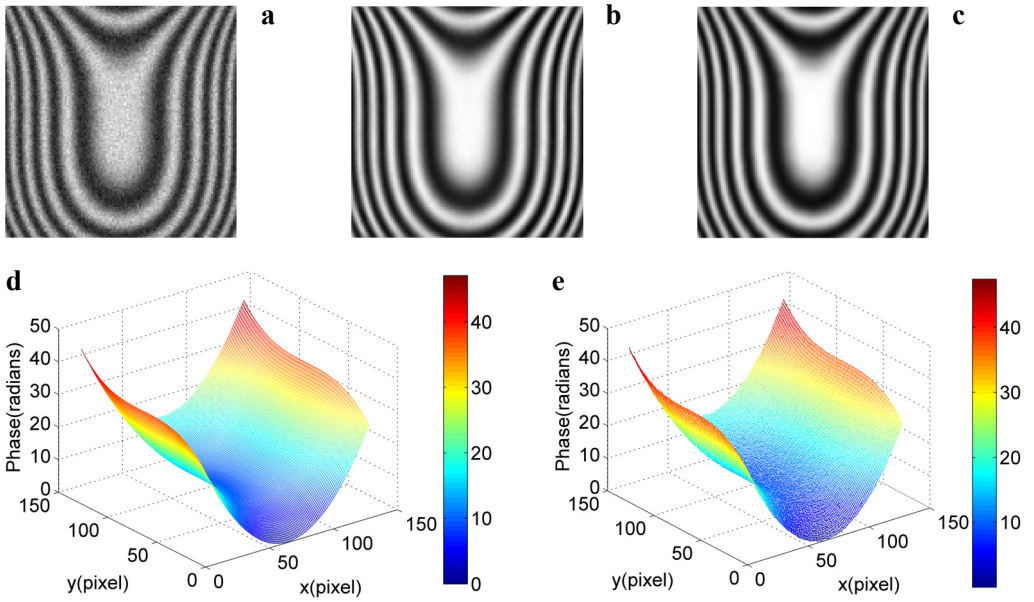

Fig. 6. The complex wave-front. (**a**) The noisy interferogram, (**b**) and (**c**) the interferograms denoised with the IBD and BM3D methods, (**d**) and (**e**) the theoretical and noisy phases, (**f**) and (**g**) the phases retrieved from the interferograms denoised with the IBD and BM3D methods, respectively.

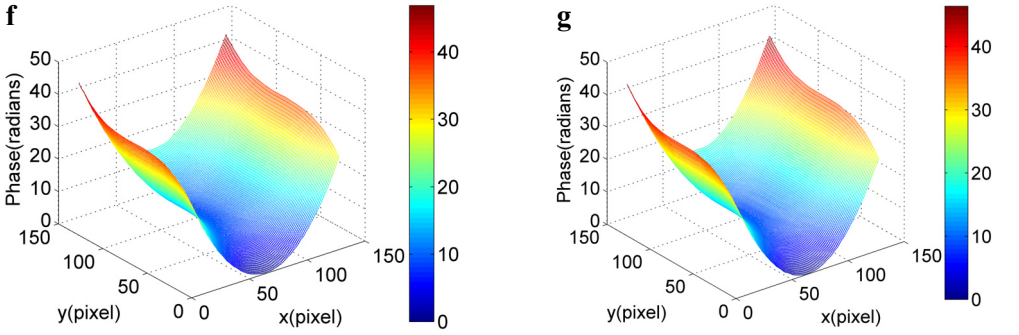

Fig. 6. Continued.

Figs. 6**d** and 6**e** is 0.1674 rad. The noisy interferograms are simultaneously denoised by the IBD and BM3D methods to achieve the noise-suppressed interferograms, one of which is shown in Figs. 6**b** and 6**c**. The phases retrieved from the noise-suppressed interferograms denoised by the IBD and BM3D methods are presented in Figs. 6**f** and 6**g**, and the corresponding RMSEs are 0.1395 and 0.1741 rad, respectively. Note that their phases are extracted by using the AIA method [24, 25].

3.3.4. The peaks

For the peaks, four noisy interferograms with 0, π/2, π and 3π/2 phase shifts, one of which is presented in Fig. 7**a**, are used to simultaneously denoise to verify the effectiveness of

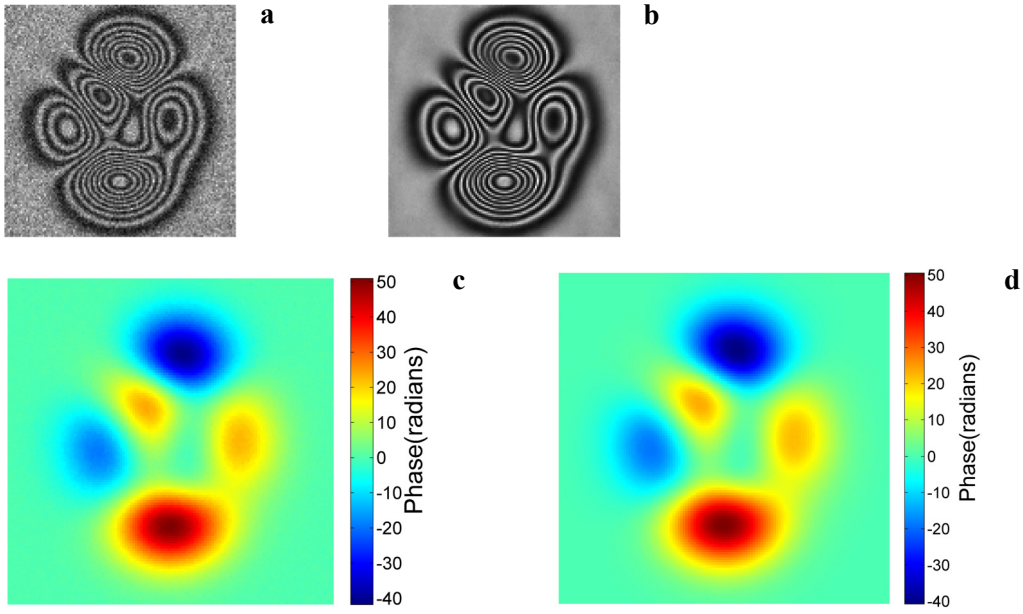

Fig. 7. The peaks. (**a**) The noisy interferogram, (**b**) the interferogram denoised with the IBD method, (**c**) the noisy phase, and (**d**) the phase retrieved from the interferogram denoised with the IBD method.

the proposed IBD method. The RMSE of the noise phase is 0.69 rad in Fig. 7**c**. The phase retrieved from the denoised interferogram with the IBD method in Fig. 7**b** is presented in Fig. 7**d**, and the corresponding RMSE is 0.39 rad and the value of noise removal for the IBD method is 0.3 rad.

From simulation results of five types of interferograms above, the advantages of the IBD method can be summarized as: 1) the IBD method can filter off the noises from not only single-frame interferogram but also multi-frame phase-shifted interferograms; 2) the IBD method has the best denoising effect, compared with the BM3D, SVD and WFF methods; 3) although the denoising effect of the IBD method for the complex wave-front and peaks is unsatisfactory, the IBD method is suitable for denoising of the plane wave-front and spherical cap.

4. Experiments

4.1. Single-frame interferogram denoising

To verify the applicability of the IBD method, we have applied this method to the real noisy interferogram with HBN (Ref. [5]), as shown in Fig. 8**a**, and the denoising result is presented in Fig. 8**b**. To compare the blind denoising performance of real interferogram denoised by the IBD approach with the other algorithms, the interferograms denoised with the BM3D, SVD and WFF methods are presented in Figs. 8**c**–8**e**, respectively. It can be seen from Figs. 8**b**–8**e** that the IBD method can provide visually satisfactory results while preserving interferogram features, compared with the BM3D, SVD and WFF methods. Compared with the real noisy interferogram, the values of

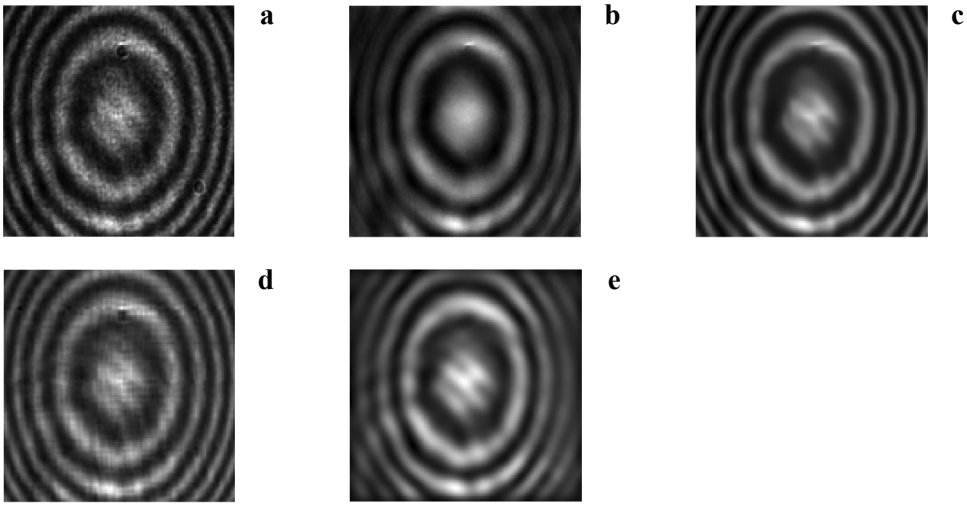

Fig. 8. (**a**) The real interferogram from Ref. [5]; (**b**), (**c**), (**d**) and (**e**) the interferograms denoised by the IBD, BM3D, SVD and WFF methods, respectively.

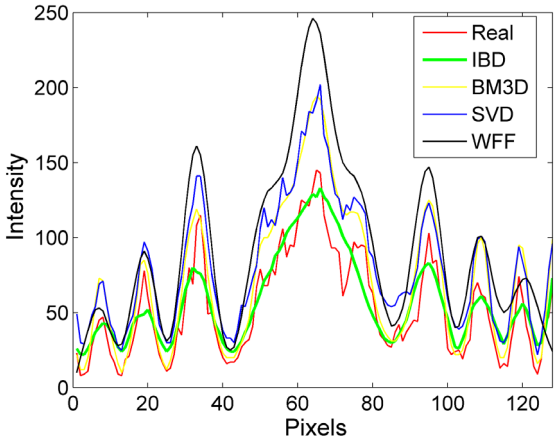

Fig. 9. The central horizontal sections of Figs. 8**a**–8**e**.

PSNR obtained with the IBD, BM3D, SVD and WFF methods are 24.26, 22.07, 19.05 and 16.54 dB, respectively. We can know that the IBD method has the highest value of PSNR. In order to further observe the contrast in details, the central horizontal sections of Figs. 8**a**–8**e** are shown in Fig. 9. From Fig. 9, it can be seen that the IBD method has successfully suppressed the multiple noise spikes of real interferogram compared with the other methods, filtering off the noises from the interferogram effectively. The experimental result demonstrates the applicability of the proposed method for single-frame interferogram.

4.2. Separating the noises from three-frame phase-shifted interferograms

To further demonstrate the practical performance of the proposed IBD method, the optical experiments of the spherical wave-front are performed. The experimental setup is similar to the Mach–Zehnder interferometer. When the phase shifts of reference wave are changed, three interferograms with random phase shifts are captured by a CMOS, respectively. The IBD method is also employed to filter off the noises from the three real interferograms with LBN, one of which is presented in Fig. 10**a**. After the three interferograms are denoised by the IBD method, one of which is shown in Fig. 10**b**. Figures 10**c** and 10**d** present the phases extracted, using the AIA method, from three real interferograms and three interferograms denoised with the IBD method, respectively. Figure 10**e** shows the phase obtained by the EVI algorithm [26] from the two real interferograms. In general, the accuracy of phase retrieval with the AIA method is higher than that of the EVI algorithm [5, 26]. To conveniently compare the accuracy of phase retrieval, the phase in Fig. 10**e** is considered as the reference phase. Through the calculation, the RMSEs in Figs. 10**d** and 10**e**, Figs. 10**c** and 10**e** are 0.23 and 0.25 rad, respectively. That is to say, the high-precision phase can be retrieved from the denoised

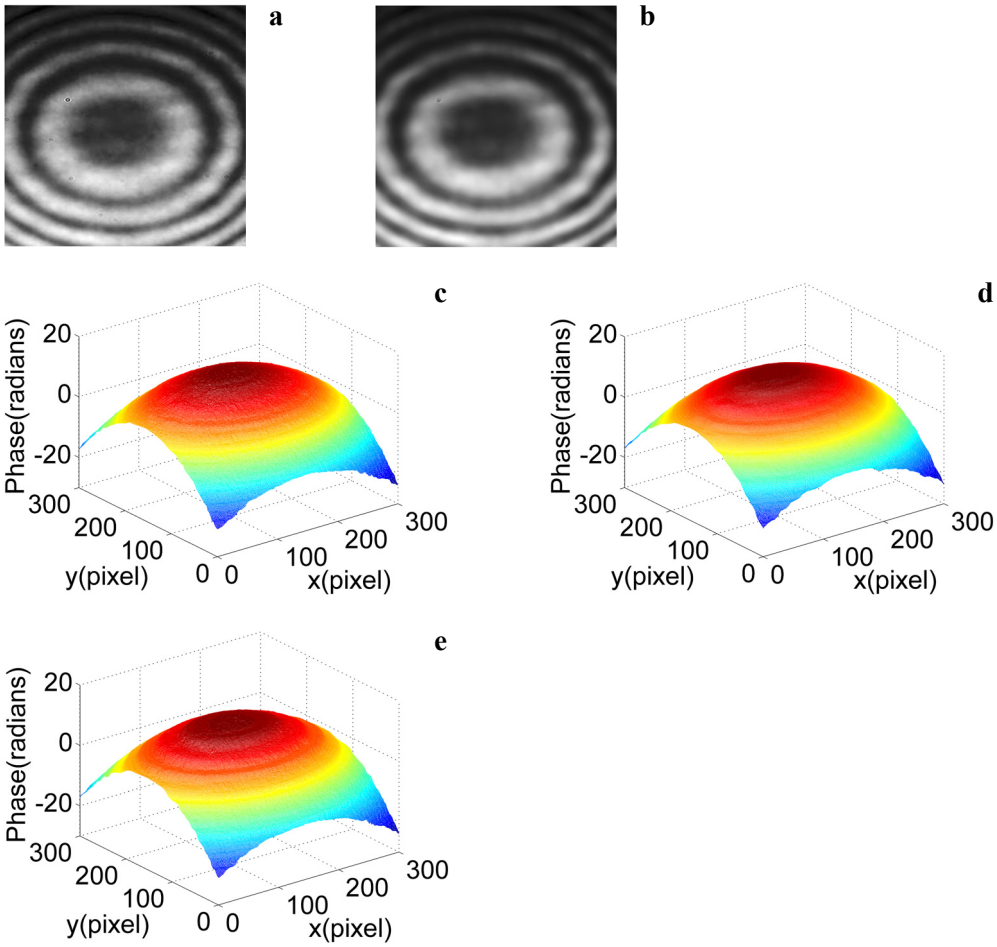

Fig. 10. (**a**) The experimental interferogram, (**b**) the interferogram denoised by the IBD method, (**c**) the phase extracted from three real interferograms, (**d**) the phase extracted from three real interferograms denoised by the IBD method, (**e**) the reference phase extracted from two real interferograms.

interferograms with the IBD method. The experimental result shows the applicability of the proposed method for collaboratively filtering multiple interferograms.

5. Conclusions

In conclusion, we have proposed a new IBD method based on DRL for denoising of phase-shifted interferogram. Based on DL, for unknown noise levels, the IBD approach is able to establish the pixel-level residual mapping relation between the interferogram and noises. The IBD method can address not only single-frame interferogram efficiently but also multi-frame phase-shifted interferograms collaboratively, and it does not require any prior evaluation about the noise levels. We have compared the IBD method

with the BM3D, SVD and WFF algorithms, and the good denoising performance of this method is demonstrated by the simulation and experimental results. The IBD method can become a useful tool and improve the accuracy of phase imaging in PSI.

Acknowledgements
This work was supported by Changzhou Sci&Tech Program (Grant No. CJ20210032), by the cultivation object of major scientific research project in Changzhou Vocational Institute of Mechatronic Technology (No. 2020ZDXM003), and by National Natural Science Foundation of China (No. 11874184).

References

[1] Yaqoob Z., Psaltis D., Feld M., Yang C., *Optical phase conjugation for turbidity suppression in biological samples*, Nature Photonics **2**(2), 2008, pp. 110–115, DOI: 10.1038/nphoton.2007.297.
[2] Xu X., Wang Y., Ji Y., Xu Y., Xie M., Han H., *A novel dual-wavelength iterative method for generalized dual-wavelength phase-shifting interferometry with second-order harmonics*, Optics and Lasers in Engineering **106**, 2018, pp. 39–46, DOI: 10.1016/j.optlaseng.2018.02.007.
[3] Xu X., Wang Y., Xu Y., Jin W., *Simultaneous measurement of refractive index and thickness for optically transparent object with a dual-wavelength quantitative technique*, Optica Applicata **46**(4), 2016, pp. 597–605, DOI: 10.5277/oa160407.
[4] Xu X., Wang Y., Xu Y., Jin W., *Dual-wavelength in-line phase-shifting interferometry based on two dc-term-suppressed intensities with a special phase shift for quantitative phase extraction*, Optics Letters **41**(11), 2016, pp. 2430–2433, DOI: 10.1364/OL.41.002430.
[5] Vargas J., Quiroga J.A., Sorzano C.O.S., Estrada J.C., Carazo J.M., *Two-step interferometry by a regularized optical flow algorithm*, Optics Letters **36**(17), 2011, pp. 3485–3487, DOI: 10.1364/OL.36.003485.
[6] Wang H., Kemao Q., Gao W., Lin F., Seah H.S., *Fringe pattern denoising using coherence-enhancing diffusion*, Optics Letters **34**(8), 2009, pp. 1141–1143, DOI: 10.1364/OL.34.001141.
[7] Qian Kemao, *Two-dimensional windowed Fourier transform for fringe pattern analysis: principles, applications, and implementations*, Optics and Lasers in Engineering **45**(2), 2007, pp. 304–317, DOI: 10.1016/j.optlaseng.2005.10.012.
[8] Fu S., Zhang C., *Fringe pattern denoising via image decomposition*, Optics Letters **37**(3), 2012, pp. 422–424, DOI: 10.1364/OL.37.000422.
[9] Vargas J., Sorzano C.O.S., Quiroga J.A., Estrada J.C., Carazo J.M., *Fringe pattern denoising by image dimensionality reduction*, Optics and Lasers in Engineering **51**(7), 2013, pp. 921–928, DOI: 10.1016/j.optlaseng.2013.02.016.
[10] Dabov K., Foi A., Katkovnik V., Egiazarian K., *Image denoising by sparse 3-D transform-domain collaborative filtering*, IEEE Transactions on Image Processing **16**(8), 2007, pp. 2080–2095, DOI: 10.1109/TIP.2007.901238.
[11] LeCun Y., Bengio Y., Hinton G., *Deep learning*, Nature **521**(7553), 2015, pp. 436–444, DOI: 10.1038/nature14539.
[12] LeCun Y., Bottou L., Bengio Y., Haffner P., *Gradient-based learning applied to document recognition*, Proceedings of the IEEE **86**(11), 1998, pp. 2278–2324, DOI: 10.1109/5.726791.
[13] Krizhevsky A., Sutskever I., Hinton G., *ImageNet classification with deep convolutional neural networks*, [In] *International Conference on Neural Information Processing Systems*, 2012, pp. 1097–1105.
[14] Shelhamer E., Long J., Darrell T., *Fully convolutional networks for semantic segmentation*, IEEE Transactions on Pattern Analysis and Machine Intelligence **39**(4), 2017, pp. 640–651, DOI: 10.1109/TPAMI.2016.2572683.
[15] Falk T., Mai D., Bensch R., Cicek O., Abdulkadir A., Marrakchi Y., Böhm A., Deubner J., Jäckel Z., Seiwald K., Dovzhenko A., Tietz O., Bosco C.D., Walsh S., Saltukoglu D., Tay T.L., Prinz M., Palme K., Simons M., Diester I., Brox T., Ronneberger O., *U-Net: deep learning for*

cell counting, detection, and morphometry, Nature Methods **16**(1), 2019, pp. 67–70, DOI: 10.1038/s41592-018-0261-2.

[16] WU Y., RIVENSON Y., ZHANG Y., WEI Z., GUNAYDIN H., LIN X., OZCAN A., *Extended depth-of-field in holographic imaging using deep-learning-based autofocusing and phase recovery*, Optica **5**(6), 2018, pp. 704–710, DOI: 10.1364/OPTICA.5.000704.

[17] XU X., XIE M., JI Y., WANG Y., *Dual-wavelength interferogram decoupling method for three-frame generalized dual-wavelength phase-shifting interferometry based on deep learning*, Journal of the Optical Society of America A **38**(3), 2021, pp. 321–327, DOI: 10.1364/JOSAA.412433.

[18] NGUYEN T., BUI V., LAM V., RAUB C.B., CHANG L.-C., NEHMETALLAH G., *Automatic phase aberration compensation for digital holographic microscopy based on deep learning background detection*, Optics Express **25**(13), 2017, pp. 15043–15057, DOI: 10.1364/OE.25.015043.

[19] HELGADOTTIR S., ARGUN A., VOLPE G., *Digital video microscopy enhanced by deep learning*, Optica **6**(4), 2019, pp. 506–513, DOI: 10.1364/OPTICA.6.000506.

[20] HE K., ZHANG X., REN S., SUN J., *Deep residual learning for image recognition*, 2016 IEEE Conference on Computer Vision and Pattern Recognition (CVPR), 2016, pp. 770–778, DOI: 10.1109/CVPR.2016.90.

[21] ZHANG K., ZUO W., CHEN Y., MENG D., ZHANG L., *Beyond a Gaussian denoiser: residual learning of deep CNN for image denoising*, IEEE Transactions on Image Processing **26**(7), 2016, pp. 3142–3155, DOI: 10.1109/TIP.2017.2662206.

[22] IOFFE S., SZEGEDY C., *Batch normalization: accelerating deep network training by reducing internal covariate shift*, arXiv:1502.03167, 2015, DOI: 10.48550/arXiv.1502.03167.

[23] NAIR V., HINTON G., *Rectified linear units improve restricted Boltzmann machines*, [In] *Proceedings of the International Conference on Machine Learning (ICML-10)*, 2015, pp. 807–814.

[24] WANG Z., HAN B., *Advanced iterative algorithm for phase extraction of randomly phase-shifted interferograms*, Optics Letters **29**(14), 2004, pp. 1671–1673, DOI: 10.1364/OL.29.001671.

[25] WANG Z., HAN B., *Advanced iterative algorithm for randomly phase-shifted interferograms with intra- and inter- frame intensity variations*, Optics and Lasers in Engineering **45**(2), 2007, pp. 274–280, DOI: 10.1016/j.optlaseng.2005.11.003.

[26] DENG J., WANG H., ZHANG F., ZHANG D., ZHONG L., LU X., *Two-step phase demodulation algorithm based on the extreme value of interference*, Optics Letters **37**(22), 2012, pp. 4669–4671, DOI: 10.1364/OL.37.004669.

Received January 4, 2021
in revised form March 20, 2021